Does N2 gas behave as a surfactant during Ag thin-film sputtering deposition? Insights from in vacuo and real-time measurements

Ramiro Zapata, Matteo Balestrieri, Iryna Gozhyk, Hervé Montigaud, Rémi Lazzari

Does N_2 gas behave as a surfactant during Ag thin-film sputtering deposition ? Insights from *in vacuo* and real-time measurements

Ramiro Zapata[a,1], Matteo Balestrieri[a], Iryna Gozhyk[a], Hervé Montigaud[a], Rémi Lazzari[1,*]

[a] *Surface du Verre et Interfaces, UMR 125 CNRS/Saint-Gobain Recherche, 39 Quai Lucien Lefranc BP 135, F-93303 Aubervilliers, France*
[b] *CNRS, Sorbonne Université, Institut des NanoSciences de Paris, UMR 7588, 4 Place Jussieu, F-75005 Paris, France*

Abstract

Circumventing the thermodynamic trend of 3D growth of noble metals on dielectric substrates to form flat continuous ultra-thin films remains a challenge for many applications involving transparent conductive layers such as photovoltaic devices or smart windows. In this context, the use of gaseous species as "surfactants" during the sputtering deposition has attracted a lot attention in the past few years. The effect of N_2 on the Ag growth on amorphous SiO_2 is revisited herein in the light of film resistivity and UV-visible differential reflectivity real-time measurements combined with *in vacuo* x-ray photoemission spectroscopy. Increasing the N_2 content in the Ar gas flow (from 0 to 40%) gives rise to a drastic decrease of the percolation threshold thickness but at the expense of film conductivity. Photoemission suggests an apparent lack of chemistry between N and Ag with the absence of N

*Corresponding author
Email address: remi.lazzari@insp.jussieu.fr (Rémi Lazzari)

in the bulk and at the surface of the Ag film despite a nitridation of the substrate due to activated species in the plasma. The plasmonic response of Ag nanoparticles evidences the dynamic presence of a N adsorbate that desorbs under vacuum once the growth is stopped. This latter decreases the metal surface energy thus inducing a flattening of islands before percolation as proved by optics. The adsorption is anisotropic between (111) and (100) facets. All of this explains (i) an earlier percolation resulting from flattened objects and a delayed coalescence, (ii) the change of film texture as seen by *ex situ* diffraction and (iii) the appearance of unfavourable grain boundaries for electrical transport in continuous films. By being immiscible in the bulk of Ag, by floating at its surface, by acting on metal surface energy and by desorbing at the end of the growth, nitrogen has all the characteristics of a "surfactant" for Ag growth.

Keywords: silver, nitrogen, thin film growth, sputtering deposition, surfactant effect, real-time monitoring, UV-vis plasmonics, photoemission

1. Introduction

The thermal insulation of buildings is a crucial lever to face the issue of global warming. In low-E or solar-control windows, complex stacks of layers are deposited by magnetron sputtering on one of the inside glass surfaces of the double-glazing [1, 2, 3]. The active layer for thermal infra-red reflection is a Ag film, the thickness (10-12 nm) of which should be well below the skin depth in the visible range to achieve optical transparency. According to the Hagens-Rubens relation [4, 5] $R = 1-2\sqrt{2\epsilon_0\omega\rho}$, the reflection coefficient R of a conductive medium at a given frequency ω is dictated by its resistivity ρ (ϵ_0

vacuum permittivity). For a fixed thickness, the remaining lever to improve the heat regulation efficiency of glazings is the film resistivity and therefore its microstructure *i.e.* the grain boundary and bulk defect densities and the quality of its interfaces. A similar issue is also encountered for metallic electrodes used in photovoltaics or optoelectronic devices such as flat display panels [6]. In this context, research efforts have been directed towards a fine tuning of the Ag deposition process to face the inherent thermodynamic trend towards 3D growth on dielectric substrates, either polycrystalline or amorphous. Mainly dictated at the first glance by the low adhesion energy of Ag on poorly-interacting supports and the large metal surface energy, even in the case of out-of-equilibrium deposition process, the so-called "Volmer-Weber" 3D growth process follows a common scenario [7, 8]: (i) the homogeneous or heterogeneous nucleation of small clusters, up to a saturation density (ii) their growth towards isolated 3D islands from direct impact or by the capture of diffusing adatoms, (iii) the coalescence of islands upon impingement with a more or less efficient recovery of equilibrium shape and a decrease of particle density, (iv) the percolation with the formation of a continuous path across the film and (iv) the filling of holes and the formation of a continuous and homogeneous film. By acting upon the first steps of the growth, it becomes possible to favour an earlier percolation and hinder the 3D growth. The relevant levers are (i) the change in nucleation density or in surface/interface energetics, the latter having a direct impact on the island equilibrium shape and (ii) the kinetics of coalescence between nanoparticles. In this context, various strategies affecting the growth of the Ag film during sputter deposition have been explored including the use of : (i) the kinetics

of deposition itself (flux and temperature) [9, 10], (ii) substrates or growth layers (ZnO in the case of Ag [11, 12]), (iii) wetting or buffer layers of transition metals [13, 14, 15, 16], of the corresponding metal oxide [17], or of Ge [18, 19, 20], (iv) film doping and alloying with metals such as Al [21, 22] and (v) gaseous species, such as O_2 [23, 24, 25, 26, 6, 27, 28, 29, 30, 31, 32] and N_2 [23, 33, 34, 35, 36, 37], during deposition.

This last strategy of gaseous "surfactants" has attracted much attention in the past few years and was recognized as an efficient pathway for producing thinner continuous Ag films even on amorphous substrates. As shown in many previous reports [24, 25, 26, 6, 27, 28, 38, 29, 30, 31, 32], O_2 addition reduces drastically the Ag percolation thickness threshold but at the expense of a film resistivity worsening due to O incorporation. This flaw can be partially circumvented by the use of N_2 that produces similar overall effects but without measurable chemical interaction with Ag [23, 33, 34, 35, 36, 37]. Nevertheless, N_2 requires higher partial pressures to achieve the same change in percolation thickness, presumably because of its lower dissociation efficiency in the plasma due the strong triple N-N bond. Beside the presence of excited N_2 molecules, plasma diagnostics actually confirm that only a small fraction of molecules is actually dissociated into atomic N [39, 40, 41]. But surprisingly, Ag films grown with N_2 addition were found free of N by *ex situ* photoemission even when using pure N_2 gas during growth [23, 42, 34, 35, 36, 37]. Nonetheless, if these findings are in line with the chemical inertness of N_2 with Ag and the lack of stable bulk Ag-nitride compounds [43], all first-principle simulations [44, 45, 46, 47, 37] report on the energetically favourable ad-

sorption of atomic N at Ag surfaces. The concomitant drastic decrease of surface energy was put forward to explain a better wetting and an earlier percolation [35, 37]. In parallel, aside from a low desorption temperature [48], experiments pointed at an unusual efficient recombinative desorption of N by direct impact (Eley-Rideal mechanism) [49, 50]. To circumvent the detrimental effect of N_2 on Ag film crystallinity while still benefiting from an earlier percolation, Jamnig *et al* [36] proposed to inject the gas only during the first stages of film growth before percolation. At last, N_2 was found to promote the [100]-Ag film texture which is an unusual orientation on a surface energy point of view for a face-centred cubic metal [42].

While N_2 appears as an efficient modifier of Ag growth leading to earlier percolation [33, 34, 35, 36, 37], the apparent lack of N in the film questions its actual floating-out surfactant behaviour that could have escaped to photoemission measurements based on depth-profiling. Also, the observed worsening of film resistivity and crystallinity remains unexplained. This work proposes to revisit the question by a combination of *in vacuo* x-ray photoelectron spectroscopy (XPS) and real-time measurements of film resistance and of surface differential reflectivity spectroscopy (SDRS). Observations are supplemented by *ex situ* x-ray diffraction (XRD) and scanning transmission electron microscopy (STEM). The objective is to unveil the effects of N_2 addition at the different stages of sputtering deposition growth of Ag on silica for a wide range of gas compositions and to discriminate between the possible origins of earlier percolation *i.e.* enhanced wetting, change in the particle density and coalescence impediment. Plasmonics is used to probe directly

particle wetting and photoemission to scrutinize N chemistry, if any, at the free surface.

2. Experimental

All experimental details regarding the film deposition and the employed techniques can be found in Ref. [31] where a similar work was performed with O_2 instead of N_2. Briefly, Ag films were grown by magnetron sputtering at room-temperature on Si wafers (thickness 280 μm, n-doped, (100)-oriented), the surface of which is covered by its $\sim$ 2 nm-thick native amorphous SiO_2 oxide. The sputtering chamber (base pressure of $< 2.10^{-8}$ mbar) includes three different two inch targets equipped with a shutter, in front of which the sample can be positioned by a manipulator. Ag depositions were carried out at a power of 50 W and a total pressure of 2 μbar in direct current mode with ultra-pure gas ($<$ 50 ppm of impurities) at a target distance of 15 cm. During Ag deposition, the total flow of Ar and N_2 gases was kept at 50 sccm while their ratio was varied via mass flow controllers. Hereafter, x%N_2 will stand for the percentage of flow of N_2 in the total. As described in Ref. [31], the deposition rates were carefully calibrated on thick films with an uncertainty of $\sim$ 1 %. For Ag, it ranged from 0.55 down to 0.45 nm.s^{-1} when increasing %N_2 from 0% to 40%. Nominal thickness is systematically used to designate the deposited amount of Ag all along this work.

Thanks to a direct connection under vacuum to an analysis chamber (base pressure $\sim 10^{-9}$ mbar) hosting an XPS apparatus, the chemistry of the free surface could be analysed without exposure to air. This capability for such

a surface sensitive tool avoids any *ex situ* depth-profiling by sputtering of capped samples that can bias the interpretation of photoemission spectra. Right after deposition ($\sim$ 20 mins), samples were analysed by recording selected core level regions (Ag 3d, N 1s, O 1s, C 1s , Si 2p). Besides a slight presence of carbon of aliphatic nature at a binding energy of $E_B = 284.5$ eV, no other contaminants, particularly implanted Ar and carbonates, were detected. As Si wafers were used as received without specific surface treatment prior to Ag deposition, the effect of plasma exposure on its surface chemistry was also explored by XPS. To decouple it from Ag deposition, wafers were exposed during 3 s to a plasma (pure Ar *i.e.* 0%N_2, and 40%N_2) ignited in radio-frequency mode on an alumina target placed not inline of sight of the sample. Due to the short duration of the substrate treatment (3 s) and the low deposition rate of this material (0.007 nm.s^{-1}), no Al was found by photoemission within the detection limit.

Real-time characterizations, namely electrical resistivity and UV-visible SDRS, were carried out simultaneously on the same substrate during Ag growth. Transport measurements allow determining (i) the electrical resistivity $\rho(t)$ as the product of the sheet resistance $R_\square$ and the film thickness t *i.e.* $\rho(t) = t \times R_\square(t)$; and (ii) the thickness at the percolation threshold t_p. Hereafter, the electrical resistivities of continuous films at a final thickness of 20 nm will be systematically compared. During a SDRS measurement, the relative variation of the sample reflectivity $\frac{\Delta R}{R}$ is recorded in the s and p polarization states of light, corresponding, respectively to an electric field perpendicular and parallel to the incidence plane. The incident angle was

fixed at 45° by the flanges of silica viewports of the deposition vessel [51, 52]. SDRS is sensitive to film morphology through the excitation of localized plasmon resonances [51, 53] in the Ag nanoparticles during the initial 3D growth stages (nucleation, growth, and coalescence). The intensities of the resulting peaks as well as their positions in energy, are driven, in a first approximation, by the aspect ratio A_r (diameter/height) of the growing objects. As already shown in details [53], the integrated SDRS signal in s polarization once normalized to film thickness t:

$$\mathcal{I}_s(t) = \frac{1}{t} \int \frac{\Delta R_s}{R_s}(\omega, t) \frac{d\omega}{\omega} \propto A_r \tag{1}$$

is a reliable reporter of the A_r evolution as both quantities are proportional to the oscillator strength of the parallel plasmon oscillation. Finally, to help rationalizing SDRS evolution upon N adsorption/desorption, the optical response of a core-shell hemisphere [54] supported on SiO_2 has been simulated with the *GranFilm* code [55] and then renormalized to Si reflection coefficient. While tabulated dielectric functions of Ag, SiO_2 and Si were used, the index of refraction of the shell was kept fixed at a value typical for nitrides ($n = 2$) [56]. The basis of this modeling are fully described in previous works [57, 58, 59, 60, 61, 62, 63, 51, 53, 54] and technical details are given in Ref. [31]. Owing to the complexity of the quantitative description of the plasmonic response and of the involved morphologies and the dielectric model limitations, simulations were kept at a qualitative level to highlight the main trends of energy shift and of change in intensity of the plasmon resonances seen in SDRS as a function of morphology. They are not meant to be quantitative in absolute values as no actual fit [60, 61, 62, 63] of SDRS spectra was attempted.

For *ex situ* measurements, Ag layers were capped with a 5 nm-thick Al-doped ZnO (AZO) film deposited by direct current from a ceramic target (target ZnO:2%Al_2O_3 in mass, power 50 W; distance 12 cm, 50 sscm and 2 μbar of pure Ar) to protect them from ageing and oxidation by contact with the atmosphere. While the AZO capping may damage the surface of the Ag film, real-time resistivity of continuous Ag films, and therefore their microstructure, do not change significantly upon capping. Thus, 20 nm-thick Ag films were analysed *ex situ* by Cu-Kα XRD in Bragg-Brentano and grazing incidence geometries (Bruker D8 Advanced and Rigaku SmartLab devices respectively); they were deposited on amorphous SiO_2 substrates (thickness 1 mm) to avoid any spurious diffraction signal from Si(100) wafer [64]. Also, in order to more accurately determine the impact of $\%N_2$ on the particle density before film percolation, AZO-capped 0.6 nm-thick Ag films were deposited on 15 nm-thick silicon nitride membranes and imaged in plane view by Cs-corrected scanning transmission electron microscopy (STEM Titan Themis from Thermo Fischer Scientific) in high angle annular dark field (HAADF) conditions. The oxidized surface of the membranes mimics that of the Si wafer. A statistical analysis, based on a "Blob-log" treatment to distinguish Ag nanoparticles from the Si wafer followed by a watershed algorithm to find the precise edges of each object, was applied to all images. All *ex situ* analyses were performed with the minimum delay after deposition while samples were systematically stored in vacuum.

3. Results

3.1. Real-time film resistivity

The percolation threshold, *i.e.* the formation of a conductive path between electrodes but before film continuity, appears as a drastic drop in film sheet resistance $R_{\square}$. Better determined as the maximum in a $\rho(t)\times t = R_{\square}\times t^2$ versus t plot [31], the corresponding equivalent thickness t_p decreases from $\sim$ 6 nm down to $\sim$ 3 nm between 0%N_2 and 40%N_2 as shown in Fig. 1-a. t_p even reaches a minimal value of 2.7 nm at 30%N_2 (Fig. 1-b, left scale). Although never directly determined, such an early percolation is in agreement with previous observations both for N_2 [34, 35, 36, 37] and O_2 [26, 27, 28, 29, 30, 31] gas addition to Ar. The decrease in t_p occurs in parallel to an increase in the continuous film resistivity at $t = 20$ nm from 6.7 to 8.5 $\mu\Omega$.cm (Fig. 1-b, right scale). Nevertheless, this 27 % increase remains much more modest than that observed for Ar/O_2 mixtures, where a change by an order of magnitude was observed between 0% to 40%O_2 (using similar deposition conditions) [31]. For those films, the strong worsening of the final film resistivity was mainly assigned to a complex formation of silver oxides and of unfavourable grain boundaries due to a change of film texture.

3.2. Photoemission analysis

To explain the above resistivity findings, the chemistry of films grown under Ar/N_2 was scrutinized using photemission. Fig. 2 shows the Ag 3d, N 1s, O 1s and C 1s core level regions [65] of 20 nm-thick Ag films. Unlike previous literature [35, 37, 36], the lack of capping layer gives direct access to the chemistry of the free surface and avoids potential desorption of species

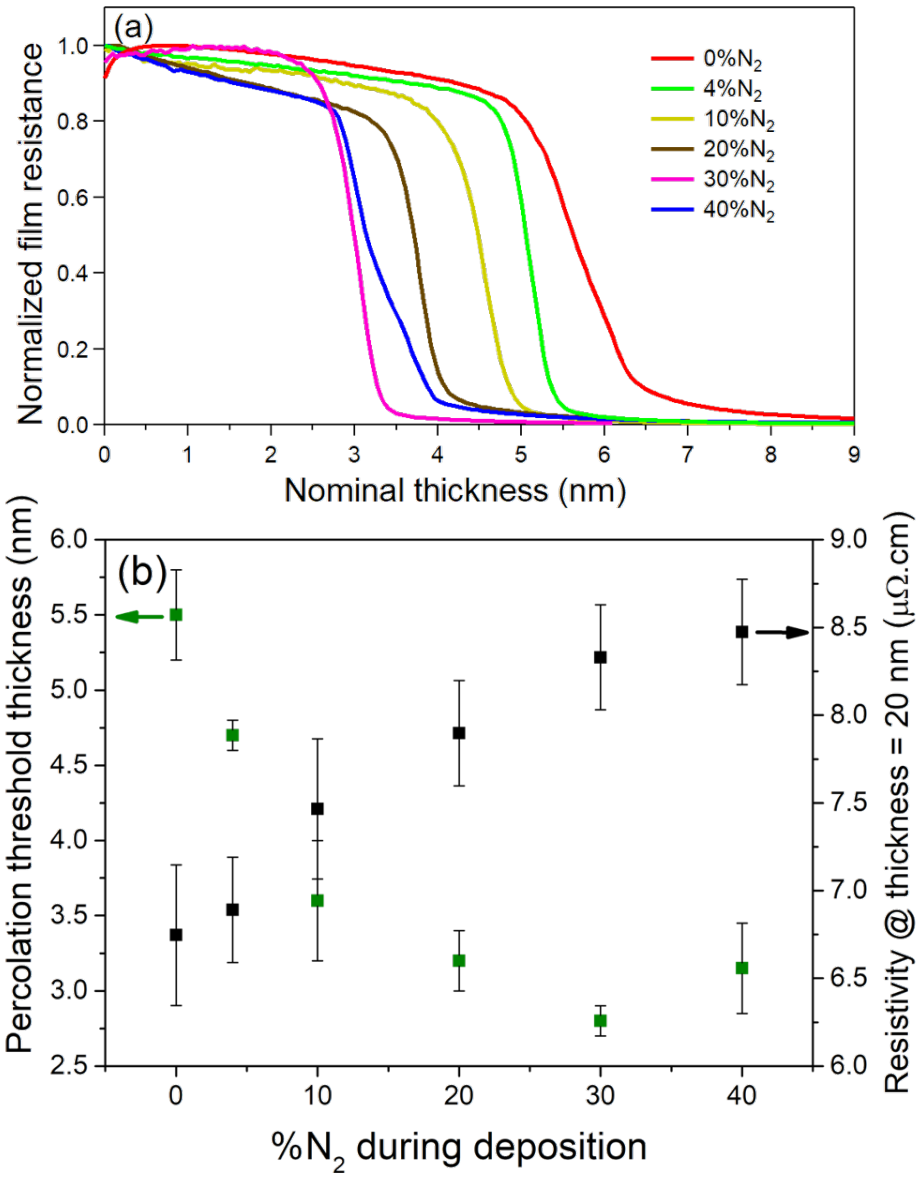

Figure 1: (a) Evolution of film sheet resistance $R_\square$ during Ag deposition on SiO_2/Si substrates as a function of equivalent thickness for different $\%N_2$ in the gas flow. Data are normalized to the initial value before opening the shutter in front the target. The drop in $R_\square$ corresponds to the formation of a percolated and conductive film. The slight increase in resistivity for some measurements at shutter opening is an artefact and does not compromise the interpretation of percolation threshold and final resistivity. (b) Percolation threshold thickness t_p (green squares, left axis) and film resistivity $\rho(t = 20\,\text{nm})$ (black squares, right axis). Values stand for an average over several (≥ 3) experiments and the error bars to the corresponding standard deviations.

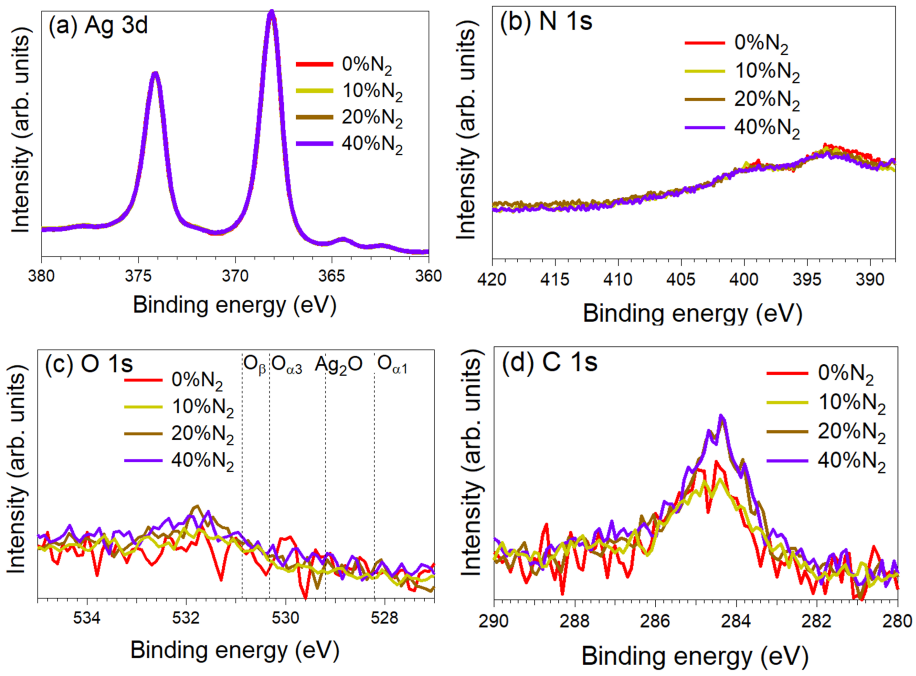

Figure 2: Photoemission analysis of 20 nm-thick Ag films after growth under different $\%N_2$ conditions. Core level regions: (a) Ag 3d, (b) N 1s, (c) O 1s, (d) C 1s. The slight bump in Fig. b corresponds to a satellite plasmon of Ag 3d core level. In Fig. b, reported peak positions for Ag-O moieties are shown [31].

induced when depositing a protective layer. For all $\%N_2$, the Ag 3d spectra (Fig. 2-a) perfectly overlap, with no change in peak position or line shape that would otherwise indicate an evolution in the chemical state of the metal. In parallel, no peak is visible in the N 1s core level range (Fig. 2-b), ruling out the presence of N in the film within the sensitivity of photoemission (*i.e.* a few % of a monolayer). These *in vacuo* observations do confirm the apparent inertness of Ag towards N suspected in previous reports [35, 37, 36] for depositions in similar conditions. It is worth noting that the plasmon multiple-loss satellite of the Ag 3d core level peak at $E_B \simeq 398 - 400$ eV should not be misinterpreted as the signature of residual traces of trapped N as done in Ref. [35]. Nevertheless, x-ray or electron induced decomposition during photoemission acquisition comparable to those observed for gold nitride [66] can not be completely ruled out despite the much shorter time scale of the measurement (a few minutes). In parallel, no significant O 1s signal that could be due to gas impurities during growth is visible (Fig. 2-c) and, only adventitious carbon contamination of aliphatic nature at $E_B = 284.5$ eV (Fig. 2-d) is present due to sample transfer (~ 20 min) despite high-vacuum conditions. At the opposite, cracking/reaction with spurious C-containing molecules during deposition would give rise to a distinct binding energy [65] characteristic of graphitic carbon ($E_B < 284$ eV) or carbonates ($E_B = 287.6 - 288$ eV). According to photoemission quantification with a model of thin film, this surface contamination amounts to a fraction of Ag(111) monolayer at the surface (see Ref. [31] for details).

Having a value of only a few nanometres at the studied photoelectron

kinetic energies [67], the probing depth of photoemission does not allow to explore the interface with the substrate in the studied 20 nm-thick films. To explore the chemical impact of the N_2-rich plasma on the wafer surface itself before Ag film percolation, the substrate was exposed during 3 s to a plasma ignited in front of an alumina target. As a reminder, such a duration corresponds to an equivalent Ag deposited thickness of ~ 1.5 nm, well below the percolation threshold. Fig. 3 summarizes the evolution before and after plasma treatment with pure Ar ($0\%N_2$) and $40\%N_2$. As seen by the shift of Si 2p (Fig. 3-a) or O 1s (not shown) core levels, all gases induces an upward band bending of about 0.4 eV. At the same time, the plasma reduces the adventitious C 1s peak of the as-introduced substrate (Fig. 3-b); this "cleaning" effect of the monolayer-thick [31] carbon contamination is more efficient with N_2 than with Ar. Similarly, at $40\%N_2$, a clear uptake of N is observed in the N 1s core level region (Fig. 3-c); it parallels a broadening of the SiO_2 component of Si 2p on the low-binding energy side that is characteristic of silicon nitride [65]. Quantification shows that such an uptake amount to about one monolayer, *i.e.* an equivalent thickness of 0.2 nm. Regardless different plasma excitations (radio-frequency for alumina versus direct current for Ag), this nitridation of the wafer demonstrates that activated N species are actually present in the plasma and that they strongly interact with the substrate surface during the time scale of film growth. This finding explains the observation in previous works of an N signal at the substrate interface by secondary ion mass spectroscopy that escaped the sensitivity of depth-profiling *ex situ* photoemission [37, 36]. However, the exact nature of these activated N-species (N atom, energetic $N^+/N_2^+, \ldots$) remains unknown.

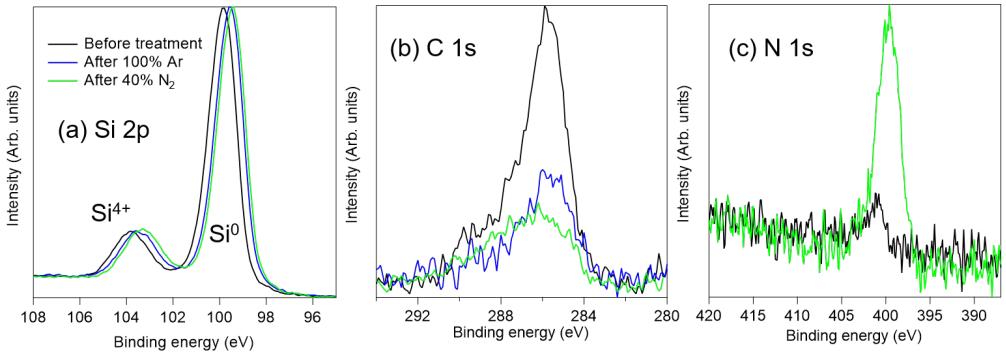

Figure 3: Evolution of Si wafer photoemission core levels after a 3 s treatment with a plasma ignited on a nearby alumina target for the indicated gas composition: (a) Si 2p, (b) C 1s, (c) N 1s.

3.3. Ex situ STEM-HAADF imaging

To get some direct insights on the influence of $\%N_2$ in the stage of discontinuous nanoparticle films, STEM-HAADF imaging was performed on AZO-capped 0.6 nm-thick Ag layers (Fig. 4). At such a thickness, all films are at the limit between growth at saturation density and the beginning of coalescence t_c that corresponds to the rise of the integrated SDRS signal $\mathcal{I}_s(t)$ [53, 31] as shown in the next section. Indeed, STEM images show the beginning of formation of elongated particles. At first sight, no clear-cut change in morphology shows up with $\%N_2$ in the images of Fig. 4, in contrast with previous reports devoted to the late coalescence regime [35, 37]. Nevertheless, image analysis revealed an increase in particle density from $4.4\,10^{12}$ to $5.7\,10^{12}$ cm^{-2} (Fig. 5). The difference could lie in the difference of substrate reactivity towards the active species in the plasma as demonstrated

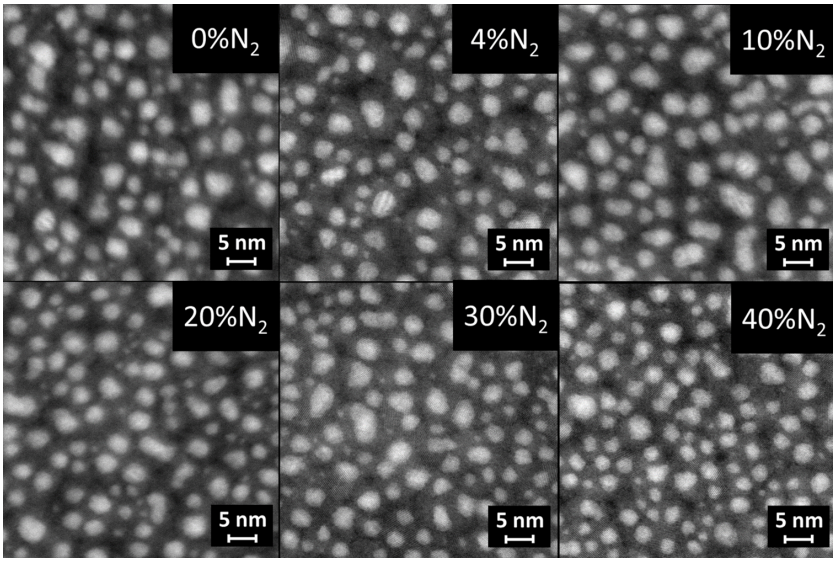

Figure 4: STEM-HAADF imaging of 0.6 nm-thick Ag films deposited on oxidized silicon nitride membranes at increasing $\%N_2$. The scale bar corresponds to 5 nm.

above by photoemission (see Fig. 3-b). Further interpretation of STEM imaging, particularly the evolution of aspect ratio, was not pursued as it may be compromised by encapsulation and uncertainties in thickness due to shutter opening/closing, at the opposite to density. Instead, the sensitivity of real-time plasmonics to wetting was exploited.

3.4. Surface Differential Reflectivity Spectroscopy

In parallel to resistivity measurements, the growth process was followed using real-time SDRS to characterize Ag nanoparticles during the initial stages of film growth. Fig. 6 shows the integrated signal $\mathcal{I}_s(t)$ in s polarization (Eq. 1) for deposition under different Ar/N_2 mixtures. For all conditions, the value of $\mathcal{I}_s(t)$ is higher than under pure Ar. This quantity being a reliable reporter of the evolution of aspect ratio A_r [53], this finding consis-

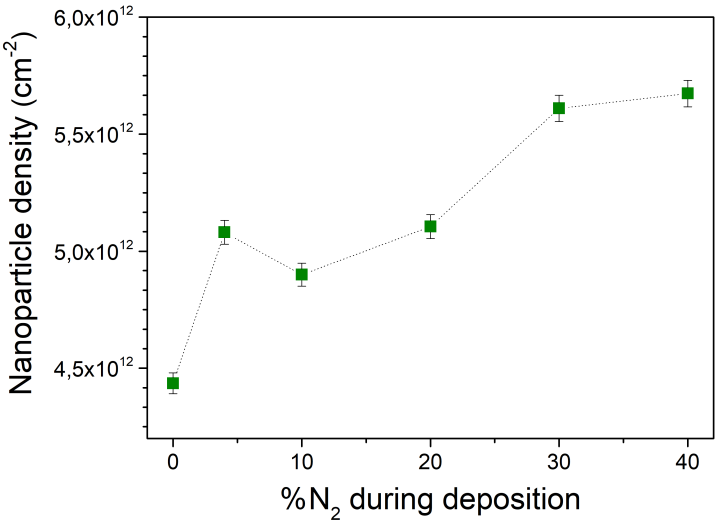

Figure 5: Evolution of the nanoparticle density with the fraction of N_2 in the gas flow. Values are deduced from STEM image analysis at the same equivalent thickness (0.6 nm). Error bars have been estimated over several images.

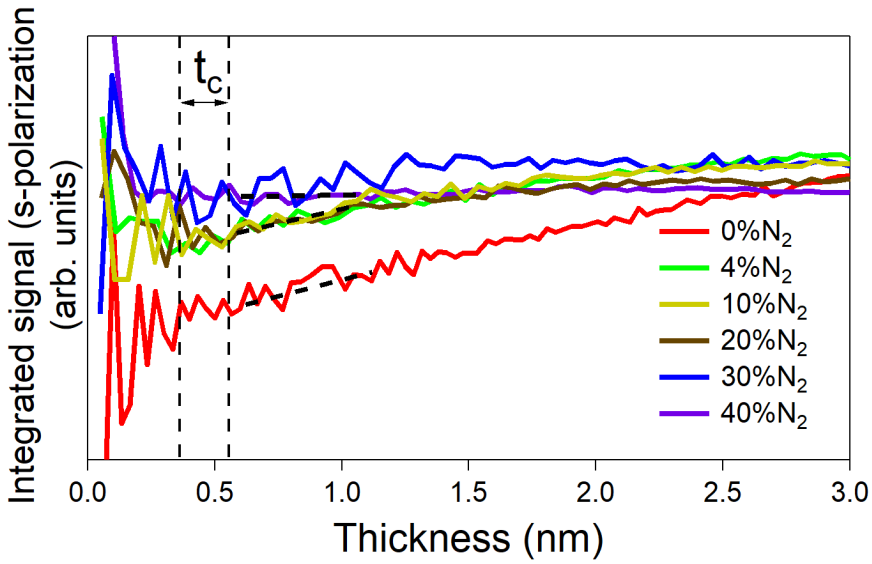

Figure 6: Integrated signal of s polarized SDRS spectra $\mathcal{I}_s(t)$ as a function of deposited equivalent thickness. The vertical line shows the approximate threshold for coalescence onset t_c while the dotted lines is a guide to the eyes showing the difference in slope in $\mathcal{I}_s(t)$ evolution.

tently indicates more flattened particles when N_2 is used despite the potential overall decrease of intensity due to the presence of an adsorbate shell (see simulations in references [31, 54] and below). Despite noise due to the division of two small quantities (see Eq. 1), this observation also holds before the onset of coalescence t_c that corresponds to the increase of the $\mathcal{I}_s(t)$ signal. Interestingly, with increasing $\%N_2$, $\mathcal{I}_s(t)$ reaches much faster the constant plateau value, which finds its origin in the competition between the increase of intensity (flattening) and the limited integration range of the red-shifted plasmon resonance [53]. The flatter particles grown with N_2 coalesce earlier than those grown without.

Fig. 7 shows the SDRS measurements in p polarization at three equiv-

alent thicknesses: 0.6 nm, 1 nm, and 2 nm. According to Figs 1 and 6, such values roughly match (i) the end of the isolated particles growth regime (0.6 nm), and (ii) more advanced particle coalescence (1 nm and 2 nm). The observed spectra are characteristic of the excitation of plasmon resonances in nanoparticles with (i) a negative dip at high photon energy associated to the dipole perpendicular to the surface and (ii) a positive feature at low energy associated to the parallel one. The latter being more sensitive to any evolution of morphology, in particular particle density, aspect ratio and formation of a core-shell structure, the discussion will mainly focus on this feature.

General trends about morphology effects on the shift and change in intensity of the plasmon resonances seen in SDRS were already predicted through dielectric simulations of the optical response of truncated spheres (see Fig. 11 of Ref. [31] and references therein). The impact of a dielectric shell on a metallic Ag core is also reminded in Fig. 8. To sum up Fig. 11 of Ref. [31], at a constant amount of metal, the low energy plasmon peak red shifts and its intensity increases upon particle flattening (*i.e.* increase of aspect ratio). A similar impact, although less pronounced than upon flattening, is found with a typical increase in particle density. The formation of a "core-shell" morphology (consisting of a shell of dielectric nature and a metallic core) strongly red-shifts the parallel resonance, whilst its intensity decreases if the shell formation is at the expense of the metallic core (Fig. 8-a versus -b). The effect is quite pronounced even for minute changes in shell thickness [31, 54] (Fig. 8), in the range of a few percent of nanoparticle radius, a change that would correspond to an atomic thickness for nano-sized particles. The shift

even strengthens with the index of refraction of the shell (not shown); its value ($n = 2$) in the present simulations was chosen somehow arbitrarily to mimic the effect a dielectric adsorbate. Thus, in principle, plasmonics is not only sensitive to an actual change in chemistry (such as an actual surface oxidation as observed in the case of O_2 [31]), but also to the presence of adsorbates in the monolayer range.

For very thin Ag films (0.6 and 1 nm; Fig. 7-a,b), the addition of N_2 leads to a red-shift, an intensity increase and a broadening of the low-energy resonance. Most of the change is nearly already set up at $4\%N_2$. According to simulations [31], this energy shift is too large to be accounted for by the change in particle density obtained from STEM pictures (Fig. 5) although it may contribute to it. On the other hand, particle flattening can explain the present plasmonic observation with $\%N_2$ and, in turn, the decrease in film percolation threshold as flattened particles with a more pronounced 2D growth would impinge on each other and form a conductive percolated network faster than more rounded 3D ones. The interpretation differs somewhat at a thickness of 2 nm (Fig. 7-c). In this case, the addition of $4\%N_2$ red shifts and enhances the low energy resonance while a further increase of $\%N_2$ keeps on shifting the peak but at the expense of its intensity and in a way nearly independent of $\%N_2$ for values greater than $10\%N_2$. This overall plasmonic scenario with $\%N_2$ matches with an increase in aspect ratio and the formation of a core-shell structure, which relative impacts on the resonance intensity are dictated by the N coverage. It also agrees with the decay on intensity of the high energy resonance with $\%N_2$ (Fig. 7 vs Fig. 8) although its red-shift

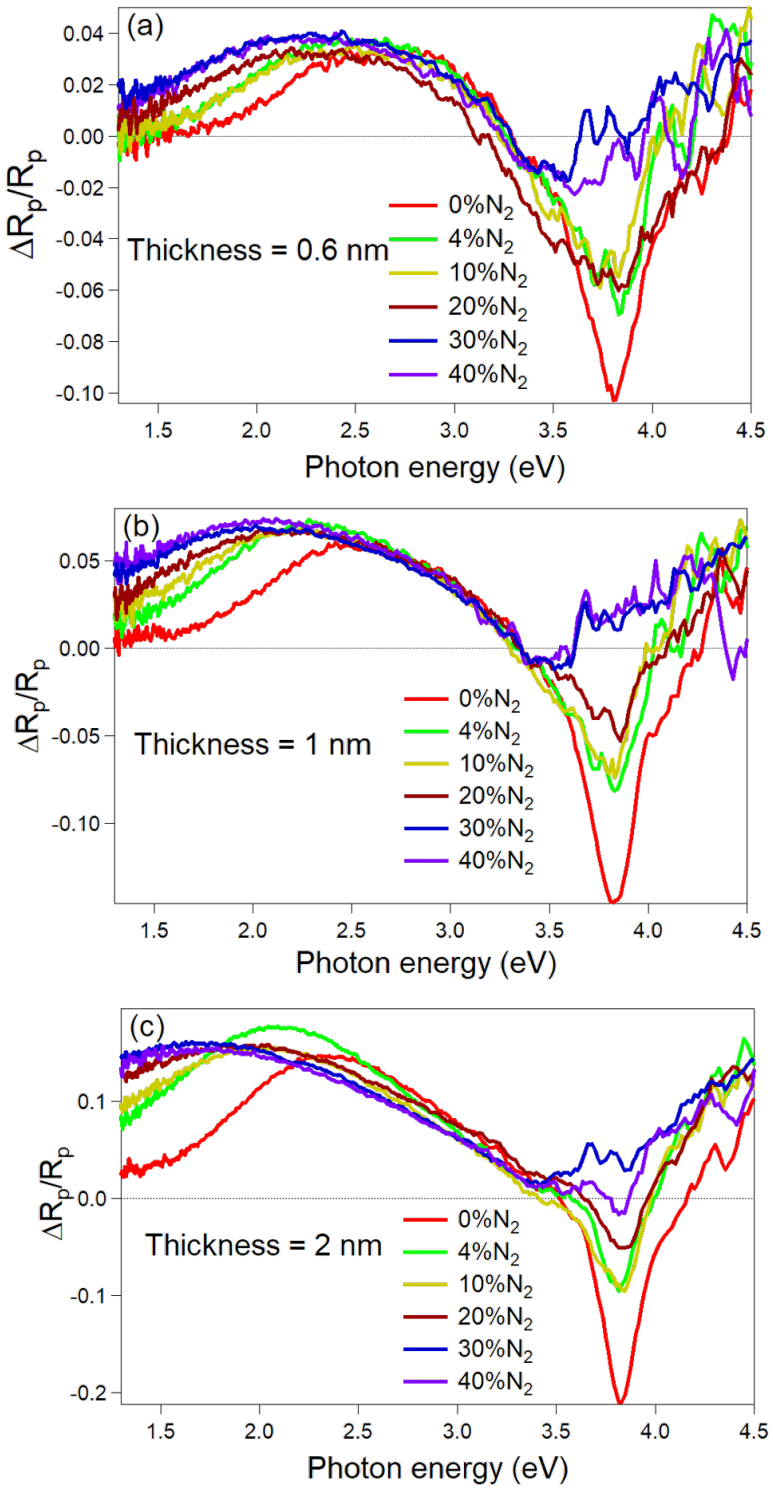

Figure 7: SDRS spectra in p polarization for different $\%N_2$ during deposition, corresponding to a nominal equivalent thickness of (a) 0.6 nm, (b) 1 nm and (c) 2 nm.

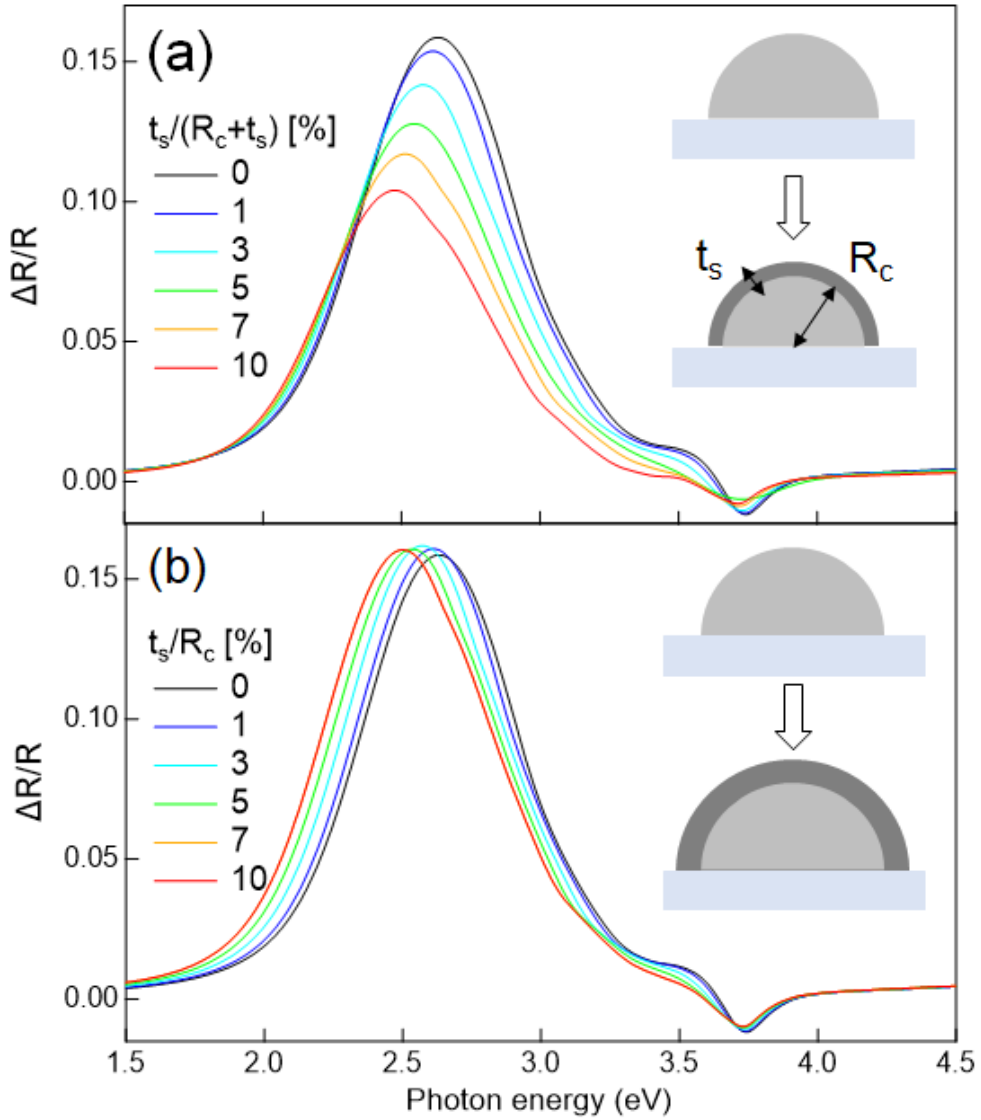

Figure 8: Simulated p polarized SDRS spectra for core-shell hemispheres arranged on a square lattice on SiO_2/Si. Evolution upon varying the shell thickness t_s at (a) the expense of the core size R_c and (b) at constant core size. The dielectric function of metallic bulk Ag was used for the core while the index of refraction of the shell was fixed arbitrarily at 2. The parallel plasmon is broadened by 0.3 eV to account for size-shape distribution and finite-size effects [31, 61, 62] and the particles are electrostatically coupled at quadrupolar order. The film thickness amounts to about 1.6 nm as in the ageing experiments of Fig. 9.

is less clear-cut due to noise. But the lack of any N 1s fingerprint for thick Ag films makes this core-shell optical scenario unlikely unless adsorbed N at the Ag surface is unstable once the growth is stopped. However, the nitridation of the wafer surface unambiguously demonstrates the presence of activated N species in the plasma, in the form of atoms or ions, that can react or be implanted. To investigate this puzzle, in-vacuum post-deposition ageing of deposits after the end of growth was investigated by SDRS.

Fig. 9 shows the evolution of SDRS spectra over an hour time scale under vacuum after gas evacuation ($p \sim 5.10^{-7}$ mbar). The cases of 1.6 nm-thick Ag films deposited under pure Ar and 20 $\%N_2$ conditions are compared. Note that spectra were corrected from the drift of the light source using an ancillary spectrometer [51]. The noticeable evolution of the spectra highlights the post-deposition film instability that is often overlooked. For the film grown under pure Ar, both resonances get closer in energy with time while their intensities poorly evolve. These trends are characteristic of a slight dewetting of nanoparticles, *i.e.* a decrease of A_r towards more rounded objects, although the slight intensity increase of the low energy resonance (Fig. 9-a and c) does not match fully theoretical expectations (see Figure 11 of Ref. [31]). Argon adsorption is obviously ruled out and an evolution of particle density by Ostwald ripening is unlikely owing to the short time scale of most of the change observed after deposition under pure Ar (a few mins; Fig. 9-a). In contrast, the evolution markedly differs at $20\%N_2$; both resonances increase in intensity and come closer in energy but with a slower evolution after the end of the growth than for $0\%N_2$. According to qualitative dielectric simu-

lations shown in Fig. 8-a (see Section 2 for all details), such a finding can only be assigned to the desorption of a N species from the surface of the nanoparticles. Indeed, dewetting cannot account, by any means, for the observed increase in intensity for both resonances, although its presence cannot be fully ruled out either. This conclusion is further reinforced by the increase with time of $\mathcal{I}_s(t)$ (Fig. 9-c); pure dewetting (*i.e.* a decrease in A_r) would give rise to the opposite (*i.e.* a decrease in $\mathcal{I}_s$). Moreover, according to Fig. 7-c, the phenomenon occurs over a time scale of 15 mins; this duration is higher than that required to transfer and analyze the sample by photoemission, thus potentially explaining the lack of traces of N in the film. Finally, as shown by comparing simulations for a shell growing at the expense of the metallic core (Fig. 8-a) or not (Fig. 8-b), the observed change of SDRS intensity upon N adorption/desorption implies a charge transfer between Ag and N, or in other words a change in the metallic character of Ag.

3.5. X-ray diffraction

Regarding film crystallography, XRD diffractograms (Fig. 10-a,b) only show, for all of the studied $\%N_2$, peaks corresponding to metallic face-centred cubic Ag, wurtzite ZnO from the capping layer, and a large feature around $2\theta = 22°$ assigned to the amorphous SiO_2 substrate. Despite the out-of-equilibrium conditions of sputtering deposition, no silver nitride formation is observed in agreement with the lack of reported bulk structure [43, 37]. First of all, as seen in the Bragg-Brentano radial scans along the out-of-plane direction (Fig. 10-a), the Ag films appears to be only [111]-[100] textured along the growth direction. Starting from the classical favoured (111) stacking under pure Ar characterized by an intense (111) peak and a weak

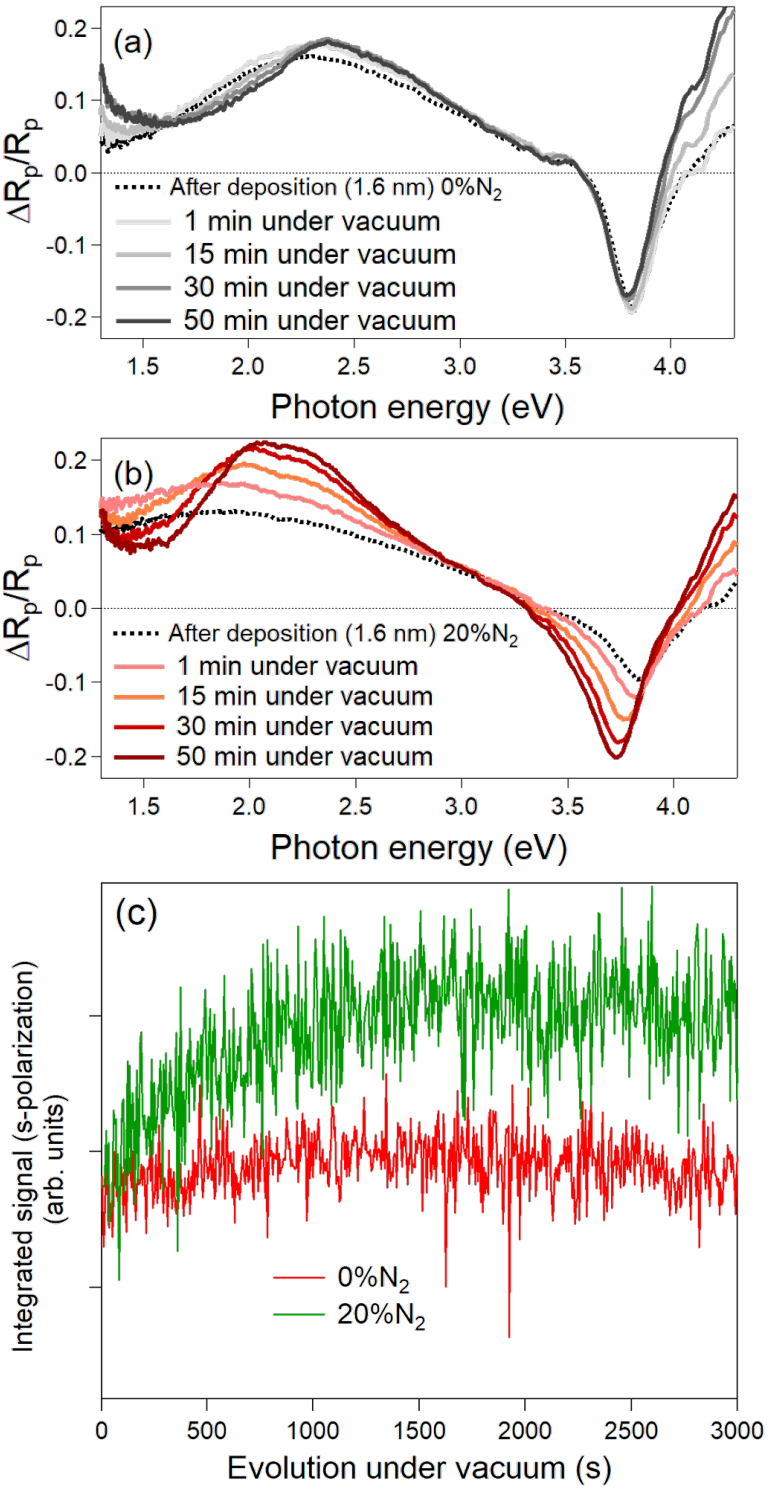

Figure 9: Post-deposition evolution under vacuum of p polarized SDRS spectra for 1.6 nm-thick Ag films deposited under (a) 0%N_2 and (b) 20%N_2. Duration after the end of the growth is indicated on figure. (c) Same evolution but for the integrated SDRS signal in s polarization (Eq. 1).

(200) reflection, the texture evolves with $\%N_2$ towards more [100]-oriented grains; this also reflects in the relative evolution of (220) and (200) peaks in the grazing-incidence scans (Fig. 10-b). Owing to the inherent poor sensitivity of Bragg-Brentano geometry at high-angles for a thin film, the lack of (220) reflection does not rule out the presence of [110] out-of-plane oriented crystallites, whose existence is supported by the (111) in-plane Bragg peak. At last, regarding the crystallites corresponding with a (311) in-plane Bragg peak (Fig. 10-b), it is impossible to assign their out-of-plane orientation with only the present set of measurement geometries. No in-plane preferential texture is expected for an amorphous substrate, a fact that is partially supported by the presence of all Ag allowed reflections in Fig. 10-b. This evolution was rationalized by fitting peaks with Voigt profiles to obtain the corresponding Debye-Scherrer sizes from full-with at half-maximum (Fig. 10-c) and an estimate of the crystallite volume fraction from peak areas (Fig. 10-d) after correction from the relative intensities as found for a powder [68] (*i.e.* from structure factors, reflection multiplicity, Lorentz-polarization factor and beam footprint). The out-of-plane Debye-Scherrer size of [111] oriented-crystallites decreases at the expense of [100] ones; but both are much smaller than the film thickness when N_2 is used thus showing a worsening of film crystallinity. Meanwhile corresponding in-plane sizes of those domains (derived from the widths of (220) and (200) Bragg peaks which normal to the corresponding diffracting planes are perpendicular to [111] and [100] directions) do not significantly change with $\%N_2$ (Fig. 10-c). In parallel to the size evolution, the film texture changes from a dominant [111] out-of-plane orientation under pure Ar to a 40/60 % [111]/[100] mix

for 40%N_2 with a minor impact in-plane (Fig. 10-d). A parallel evolution is observed in-plane on the volume fraction corresponding to (220) and (200) peaks although less pronounced due to the presence of other reflections.

4. Discussion

The addition of N_2, even in small quantities, in the Ar plasma provokes a spectacular decrease of percolation threshold (Fig. 1). Based on the previous results, on literature data and on the comparison with a similar work with O_2 [31], several aspects of this N_2 growth modifier effect can be discussed as follows.

4.1. N dynamic adsorption during growth

N_2 molecule adsorption being excluded owing to its filled orbital structure and its high bond energy, only species activated by the plasma and adsorbed at the film surface can be at the origin of the phenomenon, most probably atomic N. Indeed, N_2 ions would temporally implant as, once neutralized, the resulting molecule would immediately desorb. The N-atom hypothesis is supported by *ab initio* atomistic calculations that all predict (i) an energetically stable N adsorbate at the Ag surfaces with an adsorption energy above 2 eV/atom [44, 45, 46, 47, 37] and (ii) an energetically unfavourable dissolution in the bulk [37] in line with the strong positive enthalpy of formation of Ag nitride (314 kJ.mol^{-1}=3.25 eV/atom [43]). Thus, while the nitridation of the substrate testifies of the presence of such activated N species (Fig. 3-c), the lack of any trace of N 1s signal on thick Ag films (Fig. 2-b) can be explained only by a efficient recombinative desorption at room temperature. Indeed, photoemission (not shown) does not evidence any trace of N at the

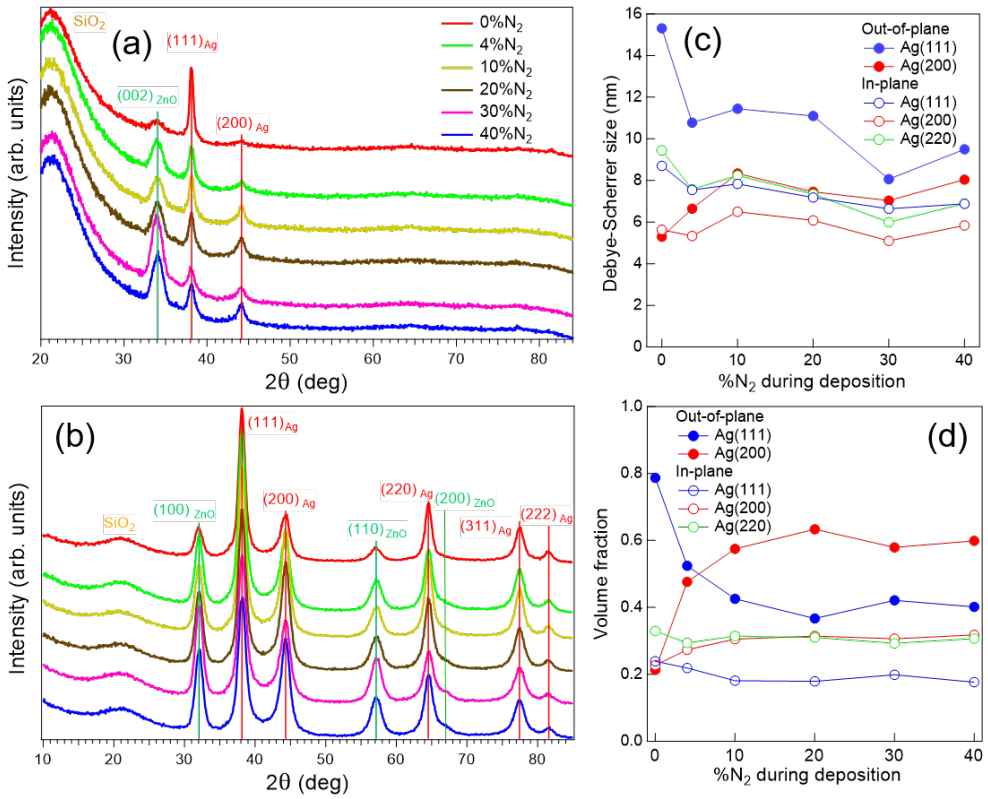

Figure 10: XRD diffractograms in (a) Bragg-Brentano and (b) grazing-incidence geometry of 20 nm-thick Ag films deposited under different $\%N_2$. Vertical bars indicate the expected bulk positions of the diffraction peaks. (c) Debye-Scherrer sizes $D = \frac{0.9\lambda}{\cos(\theta)\Delta(2\theta)}$ from peak full-width at half-maximum $\Delta(2\theta)$. Similar sizes are derived from all in-plane diffraction peaks (not shown). (d) Film texture or volume fraction from ratio of the areas of all visible peaks after correction from intensities expected from a powder sample [68].

surface of a pure 20 nm-thick Ag film exposed to a 40%N_2 plasma ignited on a alumina target during 90 s (*i.e.* more than two times the growth duration) while a slight alumina coverage of 0.07 nm is estimated by photoemission in these conditions. This points at an intrinsic N instability that is not only related to the film growth process itself. The lack of N 1s fingerprint at the Ag film surface apparently contradicts the only surface science experiment of Carter *et al.* [48] and the atomistic calculations [44, 45, 46, 47, 37] on interaction of atomic N with Ag(111) and Ag(100) orientations that all agree with a favourable adsorption. Nevertheless, a quite low recombinative desorption temperature of 350 K was found on Ag(111) [48] pointing at a poorly stable adsorbate that could be present only dynamically at the surface of Ag in the present experiments. This picture is supported by the large post-deposition evolution of SDRS plasmonic signal (Fig. 9) indicating the disappearance of a shell on top of a metallic core. In addition, the experiments of Carter *et al.* [48] on N/Ag(111) showed that the process of desorption is not of second order and therefore not limited by the surface diffusion of adsorbed N but rather by the concerted lifting of N-induced surface reconstruction and N_2 molecule desorption. Thus, the dynamic N coverage expected during growth is limited, of course by the amount of dissociation of N_2 in the plasma (*i.e.* %N_2), but also by the surprisingly reported efficient desorption of N upon direct impact of another N atom [49, 50] (*i.e.* Eley-Rideal mechanism). At last, the major difference in chemistry between the O_2/N_2 gases partly explains the much higher value of the final film resistivity at 20 nm for O_2 (80 $\mu\Omega$.cm at 40%O_2 [31]) than for N_2 (8.5 $\mu\Omega$.cm at 40%N_2; Fig. 1-b). Thus, other structural factors, such as film crystallinity, should be put forward to ac-

count for the worsening of film resistivity observed with N_2 as compared to pure Ar (Fig. 1-b).

4.2. The origins of better percolation

To rationalize the remarkable decrease of 51 % of the percolation threshold when adding N_2 (Fig. 1), the same reasoning developed for O_2 in Ref. [31] can be performed. Changes in particle saturation density ρ_s and aspect ratio A_r (diameter/height) or impeded coalescence can be put forward. Indeed, denser or flatter initial particles as well as delayed coalescence upon impingement all give rise to an earlier percolation. Assuming a scaling $t_p \propto t_c$ between the onset in thickness t_c for coalescence between nanoparticles and the electrical percolation threshold t_p, one finds:

$$t_p \propto t_c \propto D_c^3 \rho_s / A_r \tag{2}$$

where D_c is the in-plane size of particles at coalescence start. Since particles are in contact with each other at coalescence, $D_c \propto \rho_s^{-1/2}$ so that:

$$t_p \propto 1/(\rho_s^{1/2} A_r). \tag{3}$$

Then, one can estimate the expected variation of t_p from the variation of A_r and ρ_s [31] as:

$$\frac{\Delta t_p}{t_p} = -\frac{\Delta A_r}{A_r} - \frac{1}{2}\frac{\Delta \rho_s}{\rho_s}. \tag{4}$$

Thus the change in density of $\frac{\Delta \rho_s}{\rho_s} = +28$ % from 0 to 40 %N_2 found by STEM (Fig. 5) accounts only for roughly one third of the observed evolution of t_p.

Assuming equilibrium shape before coalescence, particle shape can be tackled by thermodynamics of surface/interface energies. At such sizes of a few nanometers (see Fig. 4), the scalable regime of shape as predicted by Wull-Kaischew [69] or Young-Dupré construction is achieved and energetics is not size-dependent in particular on an amorphous substrate [60, 70, 53, 71]. Unfortunately, at the opposite to evaporation [53], the SDRS signal-to-noise ratio prevents seeing the U-shaped variation of $\mathcal{I}_s(t)$, the bottom of which is characteristic of a growth at constant aspect ratio. Nevertheless, the comparison by plasmonics [63] between evaporation and sputtering growth of Ag on a similar poorly-interacting substrate (Al_2O_3) showed that equilibrium shape before coalescence is a reasonable hypothesis. Thus, the Young-Dupré equation for a truncated sphere

$$W_a = \gamma_m(1 + \cos\theta_c) \tag{5}$$

allows linking the variation of A_r to that of the contact angle θ_c, of the adhesion energy W_a and of the metal surface energy γ_m [31] through:

$$\frac{\Delta A_r}{A_r} = -\frac{\sin\theta_c \Delta\theta_c}{1-\cos\theta_c} \tag{6}$$

$$\frac{\Delta W_a}{W_a} - \frac{\Delta\gamma_m}{\gamma_m} = -\frac{\sin\theta_c \Delta\theta_c}{1+\cos\theta_c}. \tag{7}$$

Of course, forgetting cristallographic anisotropy of Ag surface energies by assuming a truncated sphere equilibrium shape [69] is a first approach of the problem that nevertheless grasps the present physics. This anisotropy

$$\left(\frac{\Delta\gamma}{\gamma}\right)_{ani} = \frac{\gamma_{(100)} - \gamma_{(111)}}{\gamma_{(111)}} \tag{8}$$

between (111) and (100) planes is modest on bare surfaces *i.e.* $\left(\frac{\Delta\gamma}{\gamma}\right)_{ani} \simeq +3\,\%$ but strongly enlarges upon N adsorption *i.e.* $\left(\frac{\Delta\gamma}{\gamma}\right)_{ani} \simeq -50\,\%$ [72, 37].

Starting from an equilibrium contact angle of $\theta_c \simeq 130°$ for Ag/SiO_2 [53, 73] and assuming that adhesion energy is not modified by the interaction of N with the substrate ($\theta_c = 130°$ for Ag/Si_3N_4 [74]), the calculated drastic decrease of Ag surface energy [37] of $\frac{\Delta\gamma_m}{\gamma_m} \simeq -75$ % for both (111) and (100) planes with N coverage would lead to a modest $\Delta\theta_c = -20°$ (Eq. 7) and $\frac{\Delta A_r}{A_r} = +16$ % (Eq. 6). So

$$-\frac{\Delta A_r}{A_r} - \frac{1}{2}\frac{\Delta\rho_s}{\rho_s} = -30\ \% \tag{9}$$

accounts only for a fraction of the observed $\frac{\Delta t_p}{t_p} = -51$ % (Eq. 4). Beyond kinetic hindrance of reshaping that could be already present during the growth of isolated nanoparticles, a delayed coalescence should be invoked to explain the remaining part of the change in t_p . Evidence of this could be found in the much faster increase of $\mathcal{I}_s(t)$ towards a plateau value in the coalescence regime (Fig. 6) when comparing deposition with and without N_2.

4.3. Anisotropic N adsorption and change in film texture

Beside the modification of surface Ag diffusion by a N adsorbate, a likely explanation of delayed coalescence can be found in the competition between the growth of [111] and [100] oriented islands, as testified by the change in film texture although XRD gives information averaged over a comparatively thicker film (Fig. 10-c). As grain boundaries between such crystallites lead to a strong structural mismatch, this explains the worsening of the final film resistivity with $\%N_2$ despite an earlier percolation (Fig. 1). Initially suggested by Kawamura *et al.* [42] to achieve films with the unusual [100] Ag orientation on an amorphous glass substrate by sputtering deposition, this surprising effect of N_2 on texture was also reported on SiO_2 upon increasing

(i) N_2 content in the gas flow in references [23, 35] or (ii) the film thickness at constant $\%N_2$ in Ref. [37]; in Ref. [36], only a loss of out-of-plane [111] texture was observed as the (200) peak is hardly visible. Assuming the dynamical presence of adsorbed N at the surface of Ag, this change in texture with $\%N_2$ matches with the calculated reversal of surface energies between N-covered (111) and (100) Ag surfaces with N surface concentration [37]. The anisotropy goes from a small value of a few % in favour of (111) (that agrees with the experimental microscopy observation of the Wulff-Kaischew equilibrium shape [72]) to around 50 % in favour of (100). Higher N_2 flow favours an enhanced N_2 dissociation and therefore a larger dynamical coverage and in turn a larger fraction of (100) facets as detected by XRD (Fig. 10-d). Similarly, when N_2 is present, Yun *et al.* [37] observed a correlation between this switch of texture and the onset of percolation. This might be explained by a kinetic competition between (i) the metal-metal aggregation by diffusion that favours an initial (111) stacking for a face-centred cubic metal, (ii) the substrate decarbonation and nitridation (see Section 3.2) and (iii) the starting of N adsorption on Ag(111) surfaces as theoretically expected on a energetic point of view at low N coverage [37]. Thus, for the Ag growth on ZnO films textured along the c-axis, N_2 gives rise to a surprising selectivity towards [111]-oriented nanoparticles (before percolation) [37]. While islands are larger in-plane due to N effect (see Section 3.4), the remarkable Ag(111)/ZnO(0001) epitaxy [12, 75], its favourable interfacial energy and the earlier percolation delay the growth of [100] orientation which is observed only for thicker films compared to the growth on SiO_2. But, during growth, as the fraction of wafer surface covered by the metal and the availability of

N or of potential (100) facets for adsorption increase, the N-covered (100) facets overcome the (111) ones. The impingement of islands with different orientations results into incomplete coalescence and earlier percolation but at the expense of poor grain boundaries for electrical transport. This scenario shows the interest in the strategy of N_2 gas deployment at the beginning of the growth to benefit from earlier percolation while avoiding the transition between orientations that is detrimental to resistivity [36]. This drawback can be turned into an advantage to grow Ag films on amorphous substrate with the unusual [100] orientation [42] or to achieve epitaxial and continuous films at very small thickness on substrates showing a cube/cube epitaxy such as MgO(001) [76].

4.4. N_2 versus O_2 as "surfactants" of Ag growth

To conclude, N_2 appears to behave as a "surfactant" during sputtering deposition of Ag. It is completely immiscible leading probably to an efficient mechanism of spillover or segregation to the surface, as already put forward in the case of O at low $\%O_2$ [28, 29, 32]. But there is no equivalent threshold of incorporation in the bulk [31] (*i.e.* of formation of subnitrides), a phenomenon that is detrimental for electrical transport in the case of O. Finally, as for O [77, 78], N adsorption decreases the surface energy of the metal thus favouring wetting. Nevertheless, the origin of N impact on the percolation threshold seems to results from a interplay between a better wetting, a change in saturation density and a delayed coalescence in which the orientation-dependent impact of N on energetics plays a decisive role.

5. Conclusion

The interpretation of the effect of N_2 during sputtering growth of Ag on an amorphous substrate was revisited using a combination of real-time and *in vacuo* measurements. Increasing the $\%N_2$ in the gas flow led to a sizeable decrease of the percolation threshold but at the expense of film resistivity. According to *in vacuo* photoemission, N is absent from the film and its surface. However, substrate nitridation and decarbonation prove the presence of activated N species in the plasma, probably atomic N that covers dynamically the metal but desorbs once the growth is stopped as indicated by the evolution of the plasmonic response. This adsorbate decreases the surface energy of the metal, thus inducing a flattening during the island growth. However, this enhanced wetting cannot explain alone the observed reduction of percolation threshold. It also involves a contribution from the change in particle density and from a delayed coalescence. The latter is assigned to the competition between [111] and [100] oriented particles that ends up in an evolution of film texture and a worsening of film resistivity. As a result, nitrogen displays all the characteristics of a "surfactant" for Ag growth. It is immiscible in the bulk of the metal, decreases its surface energy but stabilizes more (100) than (111) facets and finally desorbs easily after growth. Nevertheless, these restrictive characteristics seem specific to the case of N-Ag and could preclude, beyond the difficult dissociation of the N_2 molecule, the systematic use of such a gas as a surfactant with metals with a stronger chemical interaction with N.

6. Acknowledgments

R.Z. would like to thank Saint-Gobain Research Paris and ANRT (Agence Nationale Recherche Technologie) for his PhD funding, M.-C. Solignac (SGR/SVI) for valuable discussions about SDRS, B. Germain (SGR) for XRD measurements and L. Largeau (C2N) for his help during STEM acquisitions and the support from the ANR program of future investment TEMPOS-NANOTEM (No. ANR-10-EQPX-50).

References

[1] S. D. Rezaei, S. Shannigrahi, S. Ramakrishna, A review of conventional, advanced, and smart glazing technologies and materials for improving indoor environment, Sol. Energy Mater. Sol. Cells 159 (2017) 26 – 51.

[2] G. K. Dalapati, A. K. Kushwaha, M. Sharma, V. Suresh, S. Shannigrahi, S. Zhuk, S. Masudy-Panah, Transparent heat regulating (thr) materials and coatings for energy saving window applications: Impact of materials design, micro-structural, and interface quality on the thr performance, Prog. Mater Sci. 95 (2018) 42–131.

[3] D. Depla, Chemical stability of sputter deposited silver thin films, Coatings 12 (12) (2022) 1915.

[4] E. Hagen, F. Rubens, Connections of the reflection and emission procedure of metals to their electrical conductivity, Ann. Phys.-Berlin 11 (8) (1903) 873–901.

[5] A. E. Kaplan, Metallic nanolayers: a sub-visible wonderland of optical properties, J. Opt. Soc. Am. B 35 (6) (2018) 1328–1340.

[6] G. Zhao, W. Wang, T.-S. Bae, S.-G. Lee, C. Mun, S. Lee, H. Yu, G.-H. Lee, M. Song, J. Yun, Stable ultrathin partially oxidized copper film electrode for highly efficient flexible solar cells, Nat. Commun. 6 (1) (2015) 8830.

[7] M. Zinke-Allmang, Phase separation on solid surfaces: nucleation, coarsening and coalescence kinetics, Thin Solid Films 346 (1999) 1–68.

[8] N. Kaiser, Review of the fundamentals of thin-film growth, Appl. Opt. 41 (16) (2002) 3053–3060.

[9] V. Gervilla, G. A. Almyras, B. Lu, K. Sarakinos, Coalescence dynamics of 3D islands on weakly-interacting substrates, Sci Rep 10 (1) (2020) 2031.

[10] E. Kusano, Growth of flat-topped, mound-shaped grains with voids when depositing silver thin films at high substrate temperatures using direct-current magnetron sputtering, J. Vac. Sci. Technol. A. 40 (1) (2022) 013410.

[11] M. Arbab, The base layer effect on the d.c. conductivity and structure of direct current magnetron sputtered thin films of silver, Thin Solid Films 381 (1) (2001) 15–21.

[12] N. Jedrecy, G. Renaud, R. Lazzari, J. Jupille, Unstrained islands with interface coincidence sites versus strained islands: X-ray measurements on Ag/ZnO, Phys. Rev. B. 72 (2005) 195404.

[13] K. Fukuda, S. H. N. Lim, A. Anders, Coalescence of magnetron-sputtered silver islands affected by transition metal seeding (Ni, Cr, Nb, Zr, Mo, W, Ta) and other parameters, Thin Solid Films 516 (14) (2008) 4546–4552.

[14] N. Formica, D. S. Ghosh, A. Carrilero, T. L. Chen, R. E. Simpson, V. Pruneri, Ultrastable and atomically smooth ultrathin silver films grown on a copper seed layer, ACS Appl. Mater. Interfaces 5 (2013) 3048–3053.

[15] M. Todeschini, A. Bastos da Silva Fanta, F. Jensen, J. B. Wagner, A. Han, Influence of Ti and Cr adhesion layers on ultrathin Au films, ACS Appl. Mater. Interfaces 9 (2017) 37374–37385.

[16] M. Messaykeh, S. Chenot, P. David, G. Cabailh, J. Jupille, A. Koltsov, R. Lazzari, An *in situ* and real-time plasmonic approach of seed/adhesion layers: chromium buffer effect at the zinc/alumina interface, Cryst. Growth Des. 21 (2021) 3528–3539.

[17] G. Zhao, M. Song, H.-S. Chung, S. M. Kim, S.-G. Lee, J.-S. Bae, T.-S. Bae, D. Kim, G.-H. Lee, S. Z. Han, H.-S. Lee, E.-A. Choi, J. Yun, Optical transmittance enhancement of flexible copper film electrodes with a wetting layer for organic solar cells, ACS Appl. Mater. Interfaces 9 (44) (2017) 38695–38705.

[18] V. J. Logeeswaran, N. P. Kobayashi, M. S. Islam, W. Wu, P. Chaturvedi, N. X. Fang, S. Y. Wang, R. S. Williams, Ultrasmooth silver thin films

deposited with a germanium nucleation layer, Nano Lett. 9 (2009) 178–182.

[19] H. Liu, B. Wang, E. S. P. Leong, P. Yang, Y. Zong, G. Si, J. Teng, S. A. Maier, Enhanced surface plasmon resonance on a smooth silver film with a seed growth layer, ACS Nano 4 (2010) 3139–3146.

[20] W. Chen, K. P. Chen, M. D. Thoreson, A. V. Kildishev, V. M. Shalaev, Ultrathin, ultrasmooth, and low-loss silver films via wetting and annealing, Appl. Phys. Lett. 97 (21) (2010) 211107.

[21] H. Yan, X. Xu, P. Li, P. He, Q. Peng, C. Ding, Aluminum doping effect on surface structure of silver ultrathin films, Materials 15 (2) (2022) 648.

[22] D. Gu, C. Zhang, Y.-K. Wu, L. J. Guo, Ultrasmooth and thermally stable silver-based thin films with subnanometer roughness by aluminum doping, ACS Nano 8 (10) (2014) 10343–10351.

[23] J. F. Pierson, D. Wiederkehr, A. Billard, Reactive magnetron sputtering of copper, silver, and gold, Thin Solid Films 478 (1-2) (2005) 196–205.

[24] J. M. Riveiro, P. S. Normile, J. P. Andrés, J. A. Gonzalez, J. A. De Toro, T. Muñoz, P. Muñiz, Oxygen-assisted control of surface morphology in nonepitaxial sputter growth of Ag, Appl. Phys. Lett. 89 (2006) 201902.

[25] W. Kim, D. Ku, K. Lee, B. Cheong, Effect of oxygen content and deposition temperature on the characteristics of thin silver films deposited by magnetron sputtering, Appl. Surf. Sci. 257 (4) (2010) 1331–1336.

[26] W. Wang, M. Song, T.-S. Bae, Y. H. Park, Y. C. Kang, S. G. Lee, S. Y. Kim, D. H. Kim, S. Lee, G. Min, G. H. Lee, J. W. Kang, J. Yun, Transparent ultrathin oxygen-doped silver electrodes for flexible organic solar cells, Adv. Funct. Mater. 24 (2014) 1551–1561.

[27] G. Zhao, W. Shen, E. Jeong, S.-G. Lee, S. M. Yu, T.-S. Bae, G.-H. Lee, S. Z. Han, J. Tang, E.-A. Choi, J. Yun, Ultrathin silver film electrodes with ultralow optical and electrical losses for flexible organic photovoltaics, ACS Appl. Mater. Interfaces 10 (32) (2018) 27510–27520.

[28] G. Q. Zhao, E. Jeong, E. A. Choi, S. M. Yu, J. S. Bae, S. G. Lee, S. Z. Han, G. H. Lee, J. Yun, Strategy for improving Ag wetting on oxides: Coalescence dynamics versus nucleation density, Appl. Surf. Sci. 510 (2020) 0169–4332.

[29] E. Jeong, S.-G. Lee, J.-S. Bae, S. M. Yu, S. Z. Han, G.-H. Lee, E.-A. Choi, J. Yun, Effects of substantial atomic-oxygen migration across silver-oxide interfaces during silver growth, Appl. Surf. Sci. 568 (2021) 150927.

[30] N. Pliatsikas, A. Jamnig, M. Konpan, A. Delimitis, G. Abadias, K. Sarakinos, Manipulation of thin silver film growth on weakly interacting silicon dioxide substrates using oxygen as a surfactant, J. Vac. Sci. Technol. A. 38 (2020) 0734–2101.

[31] R. Zapata, M. Balestrieri, I. Gozhyk, H. Montigaud, R. Lazzari, On the O_2 "surfactant" effect during Ag/SiO_2 magnetron sputtering deposition:

the point of view of *in situ* and real-time measurements, ACS Appl. Mater. Interfaces 15 (2022) 36951–36965.

[32] E. Jeong, S.-G. Lee, S. M. Yu, S. Z. Han, G.-H. Lee, Y. Ikoma, E.-A. Choi, J. Yun, Spontaneous post-growth oxygen dissipation and electrical improvement of silver electrodes in substoichiometric oxidation states, Appl. Surf. Sci. 623 (2023) 156998.

[33] G. Zhao, S. M. Kim, S. G. Lee, T.-S. Bae, C. Mun, S. Lee, H. Yu, G. H. Lee, H.-S. Lee, M. Song, J. Yun, Bendable solar cells from stable, flexible, and transparent conducting electrodes fabricated using a nitrogen-doped ultrathin copper film, Adv. Funct. Mater. 26 (2016) 4180–4191.

[34] R. H. H. Ko, A. Khalatpour, J. K. D. Clark, N. P. Kherani, Ultrasmooth ultrathin Ag films by AlN seeding and Ar/N_2 sputtering for transparent conductive and heating applications, APL Mater. 6 (2018) 121112.

[35] G. Zhao, W. Shen, E. Jeong, S. G. Lee, H. S. Chung, T. S. Bae, J. S. Bae, G. H. Lee, J. Tang, J. Yun, Nitrogen-mediated growth of silver nanocrystals to form ultra-thin, high-purity silver-film electrodes with broad band transparency for solar cells, ACS Appl. Mater. Interfaces 10 (47) (2018) 40901–40910.

[36] A. Jamnig, N. Pliatsikas, M. Konpan, J. Lu, T. Kehagias, A. N. Kotanidis, N. Kalfagiannis, D. V. Bellas, E. Lidorikis, J. Kovac, G. Abadias, I. Petrov, J. E. Greene, K. Sarakinos, 3d-to-2d morphology manipulation of sputter-deposited nanoscale silvers films on weakly interacting

substrates via selective nitrogen deployment for multifunctional metal contacts, Acs Appl Nano Mater Interfaces 3 (5) (2020) 4728–4738.

[37] J. Yun, H. S. Chung, S. G. Lee, J. S. Bae, T. E. Hong, K. Takahashi, S. M. Yu, J. Park, Q. X. Guo, G. H. Lee, S. Z. Han, Y. Ikoma, E. A. Choi, An unexpected surfactant role of immiscible nitrogen in the structural development of silver nanoparticles: an experimental and numerical investigation, Nanoscale 12 (3) (2020) 1749–1758.

[38] G. Zhao, E. Jeong, S.-G. Lee, S. M. Yu, J.-S. Bae, J. Rha, G.-H. Lee, Y. Ikoma, J. Yun, Insights into effects of O-incorporated Ag nanoparticles as wetting seeds toward improving Ag wetting on oxides, Appl. Surf. Sci. 562 (2021) 150135.

[39] S. Agarwal, B. Hoex, M. C. M. van de Sanden, D. Maroudas, E. S. Aydil, Absolute densities of N and excited N_2 in a N_2 plasma, Appl Phys Lett 83 (24) (2003) 4918–4920.

[40] A. Bousquet, L. Spinelle, J. Cellier, E. Tomasella, Optical emission spectroscopy analysis of Ar/N_2 plasma in reactive magnetron sputtering, Plasma Process. Polym. 6 (2009) S605–S609.

[41] Y.-S. Liang, C. Xue, Y.-R. Zhang, Y.-N. Wang, Investigation of active species in low-pressure capacitively coupled N_2/Ar plasmas, Phys. Plasmas 28 (1) (2021) 013510.

[42] M. Kawamura, Y. Abe, K. Sasaki, Sputter-deposition of Ag films in a nitrogen discharge, Thin Solid Films 515 (2) (2006) 540–542.

[43] E. S. Shanley, J. L. Ennis, The chemistry and free energy of formation of silver nitride, Ind. Eng. Chem. Res. 30 (1991) 2503–2506.

[44] J. M. Ricart, J. Torras, J. Rubio, F. Illas, *Ab initio* cluster model study of geometry and bonding character of atomic nitrogen chemisorbed on the Cu(100) and Ag(100) surfaces, Surf. Sci. 374 (1997) 31–43.

[45] G.-C. Wang, L. Jiang, X.-Y. Pang, J. Nakamura, Cluster and periodic DFT calculations: the adsorption of atomic nitrogen on M(111) (M = Cu, Ag, Au) surfaces, J. Phys. Chem. B 109 (38) (2005) 17943–17950.

[46] D. B. Kokh, R. J. Buenker, J. L. Whitten, Trends in adsorption of open-shell atoms and small molecular fragments on the Ag(111) surface, Surf. Sci. 600 (2006) 5104–5113.

[47] B. W. J. Chen, D. Kirvassilis, Y. Bai, M. Mavrikakis, Atomic and molecular adsorption on Ag(111), J. Phys. Chem. C 123 (13) (2019) 7551–7566.

[48] R. N. Carter, M. J. Murphy, A. Hodgson, On the recombinative desorption of N_2 from Ag(111), Surf. Sci. 387 (1997) 102–111.

[49] H. Ueta, M. A. Gleeson, A. W. Kleyn, The interaction of hyperthermal nitrogen with N-covered Ag(111), J. Chem. Phys. 135 (7) (2011) 074702.

[50] M. Blanco-Rey, E. Diaz, G. A. Bocan, R. Diez Muino, M. Alducin, J. Inaki Juaristi, Efficient N_2 formation on Ag(111) by Eley-Rideal recombination of hyperthermal atoms, J. Phys. Chem. Lett. 4 (21) (2013) 3704–3709.

[51] R. Lazzari, J. Jupille, R. Cavallotti, I. Simonsen, Model-free unraveling of supported nanoparticles plasmon resonance modes, J. Phys. Chem. C 118 (13) (2014) 7032–7048.

[52] I. Gozhyk, L. Dai, Q. Hérault, R. Lazzari, S. Grachev, Plasma emission correction in reflectivity spectroscopy during sputtering deposition, J. Phys. D: Appl. Phys. 52 (2018) 095202.

[53] R. Lazzari, J. Jupille, R. Cavallotti, E. Chernysheva, S. Castilla, M. Messaykeh, Q. Hérault, I. Gozhyk, E. Meriggio, Plasmonics of supported nanoparticles reveals adhesion at the nanoscale: Implications for metals on dielectrics, ACS Appl. Nano Mater. 3 (12) (2020) 12157–12168.

[54] S. Indrehus, Plasmonics properties of supported nanoparticles, Ph.D. thesis, Sorbonne University (2020).

[55] R. Lazzari, I. Simonsen, GranFilm: a software for calculating thin-layer dielectric properties and Fresnel coefficients, Thin Solid Films 419 (1) (2002) 124–136.

[56] E. D. Palik, Handbook of Optical Constants of Solids, Vol. 1-3, Academic Press, 1985.

[57] D. Bedeaux, J. Vlieger, Optical properties of surfaces, Imperial College Press, London, 2001.

[58] I. Simonsen, R. Lazzari, J. Jupille, S. Roux, Numerical modelling of the optical response of supported metallic particles, Phys. Rev. B 61 (11) (2000) 7722–7733.

[59] R. Lazzari, I. Simonsen, D. Bedeaux, J. Vlieger, J. Jupille, Polarizability of truncated spheroidal island supported by a substrate : models and applications, Eur. Phys. J. B 24 (2001) 267–284.

[60] C. Revenant, G. Renaud, R. Lazzari, J. Jupille, Defect-pinned nucleation, growth, and dynamic coalescence of Ag islands on MgO(001): an *in situ* grazing-incidence small-angle X-ray scattering study, Phys. Rev. B 79 (2009) 235424.

[61] R. Lazzari, J. Jupille, Quantitative analysis of nanoparticle growth through plasmonics, Acs. Sym. Ser. 22 (2011) 445703.

[62] R. Lazzari, J. Jupille, Growth kinetics and size-dependent wetting of Ag/α-Al_2O_3(0001) nanoparticles studied via the plasmonic response, Nanotechnology 23 (2012) 135707.

[63] S. Grachev, M. De Grazia, E. Barthel, E. Søndergård, R. Lazzari, Real time monitoring of nanoparticle film growth at high deposition rate with optical spectroscopy of plasmon resonances, J. Phys. D: Appl. Phys. 46 (2013) 375305–375315.

[64] P. Zaumseil, High-resolution characterization of the forbidden si (200) and si (222) reflections, J. Appl. Crystallogr. 48 (2015) 528–532.

[65] J. F. Moulder, W. F. Stickle, P. E. Sobol, K. D. Bomben, Handbook of X-ray photoelectron spectroscopy, Physical Electronics, Perkin Elmer., Eden Prairie, Minnesota, USA, 1995.

[66] Y. V. Butenko, L. Alves, A. C. Brieva, J. Yang, S. Krishnamurthy,

S. L., X-ray induced decomposition of gold nitride, Chem. Phys. Lett. 430 (2006) 89–92.

[67] S. Tougaard, QUASES-IMFP-TPP2M Software, http://www.quases.com/products/quases-imfp-tpp2m/.

[68] Visualization for electronic and structural analysis, https://jp-minerals.org/vesta/en/.

[69] R. Kaischew, Sur la thermodynamique des germes cristallins., Bull. Acad., Sci. Bulg., Ser. Phys. 2 (1951) 191.

[70] R. Lazzari, J. Goniakowski, G. Cabailh, R. Cavallotti, N. Trcera, J. Jupille, P. Lagarde, Surface and epitaxial stress for supported metal clusters, Nano Lett. 16 (2016) 2574–2579.

[71] R. Lazzari, J. Goniakowski, G. Cabailh, R. Cavallotti, J. Jupille, N. Trcera, P. Lagarde, Transition from monolayer-thick 2D to 3D nano-clusters on α-al$_2$o$_3$(0001), Nanoscale 15 (2023) 15608–15618.

[72] A. Stankic, R. Cortes-Huerto, N. Crivat, D. Demaille, J. Goniakowski, J. Jupille, Equilibrium shapes of supported silver clusters, Nanoscale 5 (2013) 2448–2453.

[73] C. T. Campbell, Ultrathin metal films and particles on oxide surfaces: structural, electronic and chemisorptive properties, Surf. Sci. Rep. 27 (1-3) (1997) 1–111.

[74] M. Naka, M. Kubo, I. Okamoto, Wettability of silicon nitride by aluminium, copper and silver, J. Mater. Sci. Lett. 6 (1987) 965–966.

[75] S. Benedetti, I. Valenti, S. Valeri, S. Castilla, E. Touzé, Y. Bronstein, A. Toumar, F. Finocchi, R. Lazzari, Polar-step driven metal nucleation and growth: the Ag/ZnO($10\bar{1}0$) case, J. Phys. Chem. C 124 (2020) 6130–6140.

[76] F. Leroy, G. Renaud, A. Letoublon, R. Lazzari, C. Mottet, J. Goniakowski, Self-organized growth of nanoparticles on a surface patterned by a buried dislocation network, Phys. Rev. Lett. 95 (2005) 185501.

[77] W.-X. Li, C. Stampfl, M. Scheffler, Insights into the function of silver as an oxidation catalyst by *ab initio* atomistic thermodynamics, Phys. Rev. B 68 (2003) 165412.

[78] M. Gajdoš, A. Eichler, J. Hafner, Ab initio density functional study of O on the Ag(001) surface, Surf. Sci. 531 (2003) 272–286.